



HAL
open science

Impact of topographic obstacles on the discharge distribution in open-channel bifurcations

Emmanuel Jean Marie Mignot, C. Zeng, G. Dominguez, C.W. Li, N. Rivière,
Pierre Henri Bazin

► **To cite this version:**

Emmanuel Jean Marie Mignot, C. Zeng, G. Dominguez, C.W. Li, N. Rivière, et al.. Impact of topographic obstacles on the discharge distribution in open-channel bifurcations. *Journal of Hydrology*, 2013, 494, p. 10 - p. 19. 10.1016/j.jhydrol.2013.04.023 . hal-00840412

HAL Id: hal-00840412

<https://hal.science/hal-00840412>

Submitted on 2 Jul 2013

HAL is a multi-disciplinary open access archive for the deposit and dissemination of scientific research documents, whether they are published or not. The documents may come from teaching and research institutions in France or abroad, or from public or private research centers.

L'archive ouverte pluridisciplinaire **HAL**, est destinée au dépôt et à la diffusion de documents scientifiques de niveau recherche, publiés ou non, émanant des établissements d'enseignement et de recherche français ou étrangers, des laboratoires publics ou privés.

29

30 **1. Introduction**

31 When an urban flood occurs, streets generally carry most of the flow from the upstream to downstream part
32 of the city, especially when the area is densely urbanized (Mignot *et al.*, 2006). Flow in the streets is mostly
33 1D with mean velocities parallel to the building façades. However, in crossroads several flows collide and/or
34 separate and the flow pattern becomes complex (see Mignot *et al.*, 2008) especially when artificial
35 topographies create additional flow structures such as wakes, recirculation zones and secondary flows. Bazin
36 *et al.* (2012) have studied the impact of obstacles on a junction flow where two subcritical flows collide.
37 They observed that this impact depends on the location of the obstacles and may i) strongly modify the local
38 velocity distribution and ii) the extensions of a recirculation zone. Moreover, the authors observed that if an
39 obstacle is located within a recirculation zone, the impact of the obstacle is strongly damped.

40 Within street bifurcations, with a single inflow separating into two outflows, artificial topographies can also
41 affect the flow distribution reaching the downstream streets. The aim of the present paper is thus to
42 investigate i) the impact of obstacles on the local flow characteristics in bifurcation flows and ii) the
43 consequences of such modifications of the flow pattern on the modification of flow distribution to the
44 downstream branches. The selected artificial topographies are squared emerging obstacles which would
45 represent trees, bus-stop or any other impervious urban furniture located near crossroads.

46 The general pattern of a steady subcritical 3-branch bifurcation without obstacle is described by Neary *et al.*
47 (1999). A three-dimensional recirculating region develops in the lateral branch and secondary flows appear in
48 both outlets. The principal challenge in such separating flow lies in the prediction of flow distribution from
49 the incoming towards both outgoing flows. A review of analytical models developed to access such
50 prediction is given by Rivière *et al.* (2007). The models are based on the momentum conservation law (see
51 for instance Ramamurthy *et al.*, 1990), but Rivière *et al.* (2006) showed that this balance alone does not
52 permit to calculate the flow distribution, and that additional equations must be introduced. These authors
53 proposed an improved relationship based on i) the momentum conservation law from Ramamurthy *et al.*
54 (1990), ii) suitable stage-discharge relationships for the downstream controls in the outflow channels and iii)
55 an empirical correlation obtained through experimental data. This approach proved to accurately predict the
56 flow distribution in three-branch bifurcations in ideal conditions: 90° angle, smooth walls and identical
57 horizontal rectangular sections in each branch. Riviere *et al.* (2011) then generalized the results to 4-branch
58 intersections.

59 Nevertheless, when singularities are introduced near or in the bifurcation, the flow pattern can be strongly
60 affected and this analytical model obviously does not apply. The question raised by the present paper is to
61 what extent an introduction of single or pairs of obstacles in the vicinity of the intersection affects the
62 discharge distribution. Nine configurations of simplified square-shaped obstacles of typical size equal to 1/6
63 of the channel width are tested here. Their impact on the flow pattern and the downstream flow rates is
64 analyzed for 14 flow configurations divided in 3 series.

65 For practical reasons, velocity field for all flow configurations with all obstacles could not be measured
66 experimentally. The selected approach is rather based on a mix of experimental measurements and 3D
67 calculations. After verification of their accuracy, these calculations are considered reliable enough to support
68 the experimental investigation. In the first and second sections we describe the experimental and numerical
69 methodologies respectively along with the selected flow and obstacle configurations. In a third section, we
70 describe the impact of the obstacles on the flow pattern and discharge distribution and finally discuss the
71 impact of the base flow (before introducing obstacles) characteristics on such results.

72

73 **2. Experimental methodology**

74 **2.1 Experimental set-up**

75 The experiments were performed in the channel intersection facility at the Laboratoire de Mécanique des
76 Fluides et d'Acoustique (LMFA) at the University of Lyon (Insa-Lyon, France). The facility consists of three
77 horizontal glass channels 2m long and $b=0.3\text{m}$ wide each. The channels intersect at 90° with one upstream
78 branch (with the flow rate Q_u), one downstream branch (flow rate Q_d) aligned with the upstream one and one
79 lateral branch (flow rate Q_b). The upstream branch is connected to a large upstream storage tank where the
80 flow is straightened and stabilized by passing through a honeycomb. The flow separates in the bifurcation
81 and is finally collected by the downstream and lateral tanks. The lateral tank is connected to the downstream
82 tank and the lateral discharge Q_b is measured using an electromagnetic flow-meter (see Figure 1). When
83 pumped from the downstream tank to the upstream tank, the upstream flow-rate Q_u is measured using a
84 second electromagnetic flow-meter. In order to control the flow conditions, PVC channels (length 60 cm)
85 fitted with sharp crested weirs are added to the ends of the two exit channels so that $L_d=L_b=2.6\text{m}$ while
86 $L_u=2\text{m}$. A more detailed description of the experimental set-up can be found in (Rivière *et al.*, 2011).

87 For each flow configuration, the three boundary conditions to be set are: the upstream flow rate Q_u and the
88 height of the sharp crest weirs C_d (for the downstream branch) and C_b (for the lateral branch). The stage

89 discharge relationship (h_n, C_n, Q_n , $n=b$ or d) is calibrated experimentally for each weir: h_b and h_d are measured
90 using a digital point gauge at a length equal to 2 channel width upstream from the weirs. Similarly, the
91 upstream water depth h_u used to characterize the upstream velocity and Froude number is measured one
92 channel width upstream from the entry section of the bifurcation (see Figure 1). A point gauge is used to
93 measure backwater curves in the main and the branch channel for most flow configurations.

94 Upstream water depth h_u ranges from 25 to 71 mm and discharge Q_u from 1.6 to 7.0 L/s. The corresponding
95 Reynolds number ranges between 18000 and 65000 and the corresponding Froude number from 0.23 to 0.69.
96 Moreover, the roughness height k_s was measured using a roughness meter which revealed that the maximum
97 roughness is smaller than 1 μm and the average roughness smaller than 0.1 μm . Given the hydraulic
98 diameter, ranging from $D_h = 0.08\text{m}$ to 0.2m, the maximum relative roughness k_s/D_h is estimated to about 10^{-5} ,
99 corresponding to a hydraulically smooth regime in the Moody diagram.

100 2.2 Dimensional analysis and flow series

101 Dimensional analysis is applied to the present flow configuration. The 13 variables to be included in the
102 dimensional analysis of discharge distribution law without obstacle are the channel width b and roughness k_s ,
103 the acceleration due to gravity g , the three flow rates and associated water depths Q_u and h_u , Q_b and h_b , Q_d
104 and h_d , the two weir crest heights C_d and C_b and finally the fluid density ρ and dynamic viscosity μ .

105 5 available straightforward equations are:

106 - the mass conservation, which yields $Q_u = Q_b + Q_d$, permitting to remove the Q_d parameter.

107 - both calibrated stage discharge relationships (h_b, C_b, Q_b) and (h_d, C_d, Q_d), permitting to remove the C_b and C_d
108 parameters.

109 - the momentum balance in the bifurcation along the main flow axis (x) as proposed by Ramamurthy *et al.*
110 (1990) relating (h_u, h_d, Q_b) and thus permitting to remove the h_d parameter

111 - the empirical discharge distribution law proposed by Riviere *et al.* (2007) in their equation 2b which links
112 the discharge distribution Q_b/Q_u with h_b through three parameters: $Q_d/(b \cdot g \cdot h_d^{3/2})$, h_d/b and h_b/h_d , thus
113 permitting to remove h_b .

114 The 8 remaining variables are then $b, g, Q_b, Q_u, h_u, k_s, \rho$ and μ , including three scales, *i.e.* a time scale b^3/Q_u , a
115 length scale b and a mass scale ρb^3 .

116 Among the 5 final dimensionless parameters that rule the flow, two of them are discarded in this study. First
117 one is the Reynolds number $Re = 4\rho Q_u / [\mu(b + 2h_u)]$, as its values are reasonably high (see section 2.1) to ensure
118 fully turbulent flows. Second one is the dimensionless roughness height k_s/D_h , with D_h the hydraulic

119 diameter. As the flow regime is hydraulically smooth (see section 2.1), effect of the roughness parameter is
120 not considered hereafter.

121 The 3 final dimensionless parameters considered herein are then:

122 - the upstream Froude number $F_u = Q_u / [b \cdot h_u \cdot (g \cdot h_u)^{0.5}]$

123 - the discharge distribution parameter $R_q = Q_b / Q_u$

124 - the normalized upstream water depth h_u / b

125 These three parameters govern the flow distribution in the 3-branch bifurcation without obstacle. In the
126 sequel we investigate the impact of introducing obstacles in flows with varying value of each of these three
127 parameters at a time. The flow configurations before introducing any obstacle are labeled “0” or “base” flow.
128 Consequently, three series (S1, S2 and S3) of base flow configurations are considered in Table 1: S1 with
129 varying F_{u0} and fixed R_{q0} and h_{u0}/b , S2 with varying R_{q0} and fixed h_{u0}/b and F_{u0} and S3 with varying h_{u0}/b and
130 fixed R_{q0} and F_{u0} .

131 **2.3 Obstacle configurations**

132 For each base flow configuration (without obstacle) from Table 1, each obstacle is introduced one after the
133 other near the bifurcation as shown on Figure 2. 10 obstacle configurations are considered for each flow:
134 configuration labeled 0 is without obstacle (base); configurations labeled 1 to 7 comprise one obstacle;
135 configurations labeled 8 and 9 comprise two obstacles (obstacles 2 + 4 for configuration 8 and 2 + 6 for
136 configuration 9). The obstacles are square-shaped (section is 5x5cm), impervious, emerging (height is 20
137 cm), smooth blocks. They are led on the bottom and heavy enough to remain stable in the flow. They are
138 located at a distance of 4 cm from the closest wall and junction section (as for obstacle 5 on Figure 2) except
139 for obstacle 7 which is located at the center of the bifurcation.

140 **2.4 Methodology**

141 For each flow from Table 1:

142 - we adjusted the boundary conditions (C_d , C_b , Q_u) to obtain the desired base flow configuration without
143 obstacle (labeled “0”).

144 - we measured the corresponding discharges Q_{b0} , Q_{d0} without obstacle as shown on Figure 1.

145 - we introduced each of the 9 obstacles one after the other without changing the boundary conditions (C_d , C_b ,
146 Q_u) and in each case, we measured the downstream discharges Q_{bi} , Q_{di} , with “i” the obstacle number.

147 - we computed the indicator of discharge distribution modification corresponding to the introduction of each
148 obstacle $\Delta R_q = 100 \cdot (R_{qi} - R_{q0}) = 100 \cdot (Q_{bi} - Q_{b0}) / Q_u$, $i = 1 \dots 9$.

149 This methodology thus permits to investigate i) the impact of each obstacle on the discharge distribution for
150 each flow from Table 1 and ii) the evolution of such impact with the evolution of the characteristics of the
151 base flow (F_{u0} , R_{q0} and h_{u0}/b).

152 **2.5 Velocity fields measured through PIV**

153 In addition to discharge measurements, the horizontal velocity field is measured using PIV at a selected
154 elevation $z=3\text{cm}$ for the flow configuration in bold in Table 1. This configuration is the slowest flow from the
155 list and thus leads to the better measurement accuracy. Moreover, no PIV measurement could be performed
156 using obstacle 7 as a large portion of the intersection would be in the shade of the obstacle.

157 Polyamid particles (50 μm diameter) are added to the water which re-circulates in our closed loop. A
158 generator emitting white light through a slot is used to create a plane, 5 mm thick, light sheet at the
159 measurement elevation ($z=3\text{cm}$) in the channel junction and the branch channel. A 1280x1920 pixel
160 progressive CCD-camera with 8 mm opening objective and 25ms time-exposure connected to a PC computer
161 through a Firewire acquisition card is located above the free surface at an elevation of about 1.1 m. Inserting
162 the whole set-up in the dark finally permits to record the particle motion at the lightened elevation at a fixed
163 frame-rate of 30Hz during 133s. 4000 images are then recorded. The dimension of the measurement region is
164 350x500 mm with a horizontal resolution of 0.5 mm per pixel with 256 grey-levels. The commercial
165 software Davis (from Lavisision) permits to correct the optical distortions, to subtract the background and to
166 compute each of the 4000 velocity fields over a 15x15 mm grid, that is about 20 points per channel section.
167 The data is then averaged over the whole recording time to obtain the time-averaged velocity fields shown in
168 Figure 5.

169

170 **3. Numerical Simulation**

171 **3.1 Numerical method**

172 In the numerical model, the 3D Unsteady Reynolds Averaged Navier-Stokes (URANS) equations for the
173 conservation of mass and momentum of fluid are solved. The Reynolds stresses are represented by the eddy
174 viscosity concept and the Spalart-Allmaras (SA) model is used for the turbulence closure. The σ -coordinate
175 transformation is used to map the irregular domain with variable free-surface and bottom topography to a
176 rectangular prism. A split-operator finite difference method with non-uniform rectilinear grid is employed to

177 solve the governing equations. In each time interval, the equations are split into three steps: advection,
178 diffusion and pressure propagation. In the advection step a characteristics-based scheme is used. In the
179 diffusion step a centered difference scheme is used. In the pressure propagation step a Poisson equation is
180 derived and solved by a stable and robust conjugate gradient method CGSTAB. A comparison of the velocity
181 profiles in a bifurcation flow (without obstacle, measured by Barkdoll, 1997) computed by Li and Zeng
182 (2009) using the present SA model and by Neary *et al.* (1999) using a $k-\omega$ model reveals that the two sets of
183 results are quite similar. Further details of the present model can be found in (Lin and Li, 2002) and
184 applications of the numerical model to flow division problems in open channels were performed by Li and
185 Zeng (2010).

186 For the present application, the boundary conditions used are as follows. At the channel inlet the discharge
187 Q_u is prescribed, the velocity profile is assumed uniform and the eddy viscosity profile is specified by using
188 the mixing length model, the surface elevation gradient is set to zero and the pressure is assumed hydrostatic.
189 At both channel outlets the water depth and the discharge are related by the experimental weir equations
190 (h_b, C_b, Q_b) and (h_d, C_d, Q_d) and the streamwise gradients of the pressure and of the three velocity components
191 are set to zero. At the free surface, the pressure is assumed atmospheric (zero relative pressure), the gradients
192 of the velocity components are set to zero and the free surface elevation is tracked by solving the kinematic
193 equation. At solid boundaries (channel walls and obstacles) the normal gradients of pressure and velocity are
194 set to zero, and the velocity components along the boundaries are specified by the standard wall function,
195 considering smooth walls. All 14 flow cases given in Table 1 with the base (no obstacle) and 9 obstacle
196 configurations are replicated in the numerical simulation. The grid system used is rectilinear and non-
197 uniform, with the finest grid size used near solid boundaries. The total number of grid points is 182160.

198 **3.2 Validation of numerical method**

199 A comparison between the computed and measured outlet discharges for all flow configurations using each
200 obstacle configuration is given in Figure 3. The results are accurate, the difference between the computed and
201 corresponding measured downstream outlet discharges is generally within 5% of the inlet discharge. This
202 gives confidence regarding the model capacity to predict the flow distribution. Moreover, Figure 4 presents a
203 comparison of measured and computed water depth evolution along the main channel for the reference flow
204 configuration (see * in Table 1) without obstacle and with obstacle 7. The results are generally satisfactory
205 and within 5% difference of the water depth. Nevertheless, the computed outlet water depth without obstacle
206 is slightly higher than the measurements. Indeed, in the present case the downstream discharge is slightly
207 overestimated by the calculation and thus, using the downstream stage-discharge relationship, the

208 corresponding water depth is also overestimated. Overall, the tendency remains similar. Regarding the case
209 with obstacle 7, the discharge distribution is fairly estimated and thus also the downstream backwater curve,
210 but the computed head loss in the intersection is slightly lower than the measured one. Moreover, grid
211 refinement study was carried out. The number of grid points used in the fine grid system was four times of
212 that used in the original grid system. The corresponding computed backwater curves are shown in Fig. 4. The
213 maximum difference between the two set of results is approximately 2%. The discharge distribution and the
214 velocity profiles at various locations were also compared in Table 2. The difference in the discharge
215 distribution is within 3%. Finally, the sensitivity of the solution to the inlet velocity profile was also studied:
216 the replacement of the uniform velocity profile by a logarithmic profile only marginally affects the solution
217 (see Figure 4), showing that the length of the upstream channel is sufficiently long to eliminate inlet effects.

218 Finally, a comparison of five measured and computed velocity field in the intersection region for the bold
219 flow from Table 1 is included in Figure 5: without obstacle (O_0) and with obstacles 1, 2, 4, 5. As computed
220 data results from unsteady numerical simulations, a time-averaging process was applied to the computed data
221 for a better comparison with the time-averaged measured data. The magnitude of the velocity is generally
222 satisfactorily predicted, except for the accelerated upstream flow near the right bank for obstacle 2. To
223 conclude, the numerical model is considered as validated. In the sequel, the analysis of the impact of
224 obstacles on the flow pattern is performed both from experimental and numerical data.

225

226 **4. Results**

227 Measured and computed velocities (Figure 5) and depths (Figure 6) reveal that the obstacles cause pile up of
228 water immediate upstream and generate downstream wake regions with recirculating flows, leading to flow
229 and streamline deflections. In the first subsection the impact of the obstacles on a selected flow (“PIV
230 measured flow” in Table 1) is analyzed and in the three following sub-sections, the influence of the base flow
231 characteristics from each serie in Table 1 on the obstacle impact is discussed.

232 **4.1 Impact of the obstacles on the flow pattern and discharge distribution on a selected flow**

233 Considering the PIV measured base flow (bold in Table 1) and using Figures 5, 6, 7 and 8, it is observed that:

234 - Without obstacle, the main flow is separated into two parts by the plane interface. The velocity along x axis
235 thus decreases within the intersection. Maximum velocity along y axis is encountered in the lateral branch
236 along the left bank wall while a recirculation zone is observed along the right bank wall. The water depth

237 increases from the junction to the downstream branch while it decreases toward the lateral branch (see Figure
238 6). This behavior is in fair agreement with flow description in the literature by Neary *et al.* (1999)

239 - Introducing obstacle 1 strongly accelerates the right part of the upstream flow ($-150\text{mm} < y < -300\text{mm}$) in the
240 section. Due to the increased momentum (inertia), the capacity of the flow to rotate towards the lateral branch
241 is strongly reduced and the discharge in the lateral branch decreases ($\Delta R_q < 0$ in Figure 7).

242 - Introducing obstacle 2 deflects a large portion of the upstream flow towards the opposite wall ($y=0$) where
243 it is accelerated. This reduces the flow entering the lateral branch ($\Delta R_q < 0$) and causes a reduction in the water
244 depth in the lateral branch.

245 - Introducing obstacle 3 does not affect the flow pattern nor the discharge distribution as it is located within
246 the very slow recirculation zone (dead zone, see Figure 8).

247 - Introducing obstacle 4 dramatically limits the section of the mean flow in the lateral branch near the
248 downstream wall ($0.2\text{m} < x < 0.3\text{m}$ and $-0.6\text{m} < y < -0.3\text{m}$). The branch discharge is thus reduced ($\Delta R_q < 0$) and the
249 flow pattern within the branch is also strongly modified.

250 - Introducing obstacles 5 and 6 limits the flow section in the downstream branch, causes pile-up of the
251 junction water depth, which tends to increase the discharge in the lateral branch ($\Delta R_q > 0$).

252 - Introducing obstacle 7 tends to accelerate the flow along x axis within the junction on both sides of the
253 obstacle (see Figure 8). The part of inflow deflected to the left bank ($y > -150\text{mm}$) reaches the downstream
254 branch while the part deflected to the right bank is itself separated in two parts, each part reaching one outlet
255 channel. The deflection towards right side enhances the flow reaching the lateral branch and thus leads to
256 $\Delta R_q > 0$.

257 To conclude, it appears that both upstream obstacles (1 - 2) lead to $\Delta R_q < 0$ while both downstream obstacles
258 (5 - 6) lead to $\Delta R_q > 0$. Oppositely, impact of both lateral obstacles (3 - 4) on ΔR_q differs. Moreover, Figure 7
259 reveals that the impact of introducing obstacle configurations 8 (resp. 9) is about the sum of the impacts of
260 the constituting obstacles, that is of obstacles 2+4 (resp. 2+6).

261 **4.2 Impact of the inflow Froude number: F_{u0} (Serie 1)**

262 Figure 7 reveals that the sign (positive or negative) of ΔR_q for a given obstacle does not change with varying
263 Froude number of the base flow: none of the curves crosses the $\Delta R_q = 0$ axis. It appears that as the Froude
264 number of the base flow increases, the impact of each obstacle raises: $|\Delta R_q|$ increases. Indeed, the Froude

265 number is the square root of the ratio between inertia force and gravity force. So, as the resistance force (drag
266 force) produced by the flow on an obstacle is proportional to the square of the flow velocity, the increase in
267 flow inertia leads to an increased resisting force on the obstacles. In return, as the Froude number of the flow
268 increases, the pile-up at the stagnation point in front of the obstacle and the intensity of the wake increase.
269 Both processes affect the flow pattern and thus the obstacle impact is enhanced. Moreover, Figure 7 reveals
270 that for the flows studied in Serie 1, magnitude of discharge distribution modification ranges between less
271 than 5% for the low Froude number configurations to a maximum of 10% for the highest Froude number.
272 Modifications are then limited for all flow and obstacle configurations.

273 **4.3 Impact of the base discharge distribution: R_{q0} Series 2**

274 Figures 8 and 9 show the impact of introducing obstacles in flows which base discharge distribution R_{q0}
275 (without obstacle) varies between 0.2 and 0.8. Experimentally, increasing R_{q0} with constant F_{u0} and h_{u0}/b is
276 obtained by keeping the same upstream discharge Q_u and water depth h_u and by increasing (resp. decreasing)
277 the weir crest height in the downstream channel C_d (resp. branch C_b). Thus for constant upstream flow
278 conditions, varying R_{q0} affects (see Figure 8): i) the location of the interface-plane which separates the
279 upstream flow into a left portion reaching the downstream branch and a right portion reaching the lateral
280 branch, ii) the width of the recirculation region in the branch and iii) the tendency of the downstream flow to
281 detach from the left bank ($y=0$) and to initiate a recirculation zone in the downstream branch. Assuming a 2D
282 flow, the interface between both inflows starts in the upstream branch and ends at the downstream corner of
283 the junction. For $R_{q0}=0.5$, the upstream limit of the interface plane is located at the centerline of the upstream
284 branch ($x<0$, $y=-b/2$), while for $R_{q0}<0.5$ this plane starts at $y<-b/2$ and for $R_{q0}>0.5$, it starts at $y>-b/2$.
285 Tendencies of ΔR_q for increasing R_{q0} with the nine obstacles are summarized in Table 3. The relative location
286 of this interface and each obstacle permits to explain most results:

287 - For low R_{q0} , the interface is located near the lateral branch side and thus far from **obstacle 1**. As obstacle 1
288 then tends to accelerate the flow, its rotation capacity towards the lateral branch decreases: $\Delta R_q < 0$ (see
289 section 4.1). For increasing R_{q0} , the interface starts closer to obstacle 1 and part of upstream flow deflected to
290 the right side of the obstacle passes to the right side of the interface of the base flow and finally reaches the
291 lateral branch. Consequently, the $\Delta R_q < 0$ tendency described above decreases as R_{q0} increases.

292 - Oppositely, as R_{q0} increases the interface plane goes away from **obstacle 2** and the discharge distribution
293 becomes less influenced by the obstacle: $|\Delta R_q|$ decreases. It should be noted that for very low R_{q0} , the base
294 flow interface plane becomes located very close to the right bank of the inflow and thus the part of the flow

295 deflected by obstacle 2 to the right side of the inflow leads to an increase of ΔR_q compared to slightly higher
296 R_{q0} (see Figure 9).

297 - **Obstacle 4** is located in the major flow zone of the branch channel. Its blockage effect increases with the
298 lateral outflow discharge, that is as R_{q0} increases.

299 - **Obstacles 5 and 6** tend to block the flow in the downstream channel and thus to increase the branch
300 discharge (see section 4.1). However, for increasing R_{q0} values, the discharge in the downstream channel
301 decreases and thus also the velocity at this section. Corresponding pile-up and adverse pressure gradient thus
302 decreases. Consequently, introducing obstacles 5 and 6 always leads to $\Delta R_q > 0$ but this impact decreases as
303 R_{q0} increases.

304 - For R_{q0} lower or close to 0.5, **obstacles 7** tends to deflect most of the right part of upstream flow towards
305 the branch side leading to $\Delta R_q > 0$ (see section 4.1 and Figure 8). At the same time, the acceleration in the
306 downstream channel suppresses the flow separation at the left bank. However, for R_{q0} much larger than 0.5,
307 part of the flow which reached the lateral branch when no obstacle was included is now deflected by obstacle
308 7 towards the left wall ($y=0$) and finally reaches the downstream channel. As a consequence, for very high
309 R_{q0} , obstacle 7 benefits the downstream channel and $\Delta R_q < 0$.

310 - **Obstacle configurations 8 and 9** follow the same trend as their constitutive obstacles (2+4 for obstacle 8
311 and 2+6 for obstacle 9).

312 - The impact of **obstacle 3** is related to the recirculation width in the lateral branch. According to Figure 8, as
313 R_{q0} increases, the width of the recirculation region in the lateral branch decreases and thus **obstacle 3** tends to
314 pass from the recirculation zone to the main flow. As a consequence, for high R_{q0} , obstacle 3 tends to block
315 off part of the lateral branch flow (increasing the water depth and creating an adverse pressure gradient),
316 leading to $\Delta R_q < 0$.

317 **4.4 Impact of the normalized water depth: h_{u0}/b (Serie 3)**

318 Figures 10 and 11 show the influence of the upstream water depth of the base flow h_{u0} on the impact of each
319 obstacle. First, it appears that the effect of water depth on the change in flow distribution is negligible except
320 for the 3 configurations involving obstacle 2 (configurations 2, 8 and 9) where it still remains limited. For
321 these configurations, as the base water depth increases (with similar Froude number and discharge
322 distribution), the discharge in the branch is reduced: $\Delta R_q < 0$ decreases until a minimum value for $h_{u0}/b \sim 0.18$
323 and then increases again for higher water depths. Numerical results in Figure 10 show that varying the water

324 depth h_{u0} affects the wakes generated downstream from obstacles 1 and 2, even though all our experiments
325 belong to the “vortex street” flow type, when following Chen & Jirka (1995) approach. Indeed, the wake
326 parameter $S=f.a/(4h_u)$ ranges from 0.003 to 0.013 (*i.e.* $S<0.2$), with $a=0.05\text{m}$ the obstacle width and f the
327 Darcy-Weisbach coefficient ranging from 0.02 to 0.027 considering smooth walls in our experiments. For
328 obstacle 1, the wake modification hardly affects the discharge distribution (see Figure 11) as the obstacle is
329 located far from the separation streamline. Oppositely, for obstacle 2, the wake modification appears to be
330 responsible for the modification in discharge distribution for configurations 2, 8 and 9. This information
331 revealed by the numerical results proves the interest of coupling experimental and numerical data for the
332 analysis.

333

334 **5. Discussion and Conclusion**

335 The aim of the present paper was to investigate how the flow is affected by obstacles located in a 3-branch
336 bifurcation with specific attention towards the impact on the discharge distribution to the downstream
337 branches. Two types of measurements were undergone: i) discharge distribution measurements for 14 flows
338 belonging to three series in which only one main parameter of the flow was varying at a time and in which 9
339 obstacles were introduced one after the other; and ii) horizontal velocity field for one selected flow with most
340 obstacle configurations using PIV techniques. In parallel all flows with all obstacle cases were computed
341 using a CFD approach. Combination of both experimental and numerical approaches permitted to explain the
342 outlet discharge modifications induced by obstacles by analyzing the changes in the flow pattern. The
343 following conclusions can be outlined:

344 - The computation results of the numerical model in terms of outlet discharges and flow field are in
345 fair agreement with measurements and thus this CFD model represents a suitable predictive tool to further
346 study localized urban flooding configurations where the flow is strongly complex and 3D.

347 - The impact of an impervious obstacle on the discharge distribution in a subcritical 3-branch
348 bifurcation flow is strongly dependent on the location of the obstacle with regards to the intersection.
349 Obstacles located within the upstream branch increase the streamwise flow velocity and thus tend to reduce
350 the lateral and increase the downstream discharge (Rq_0 decreases up to 12%). Oppositely obstacles located
351 within the downstream branch tend to block off the flow in this branch and to reduce the corresponding
352 discharge while increasing the lateral discharge (Rq_0 increases up to 3%). Finally for obstacles located within
353 the lateral branch, their impact depends on the side of the channel in which they are introduced: i) towards
354 the downstream wall of the lateral branch, they tend to block off the lateral flow and thus promote the

355 downstream and reduce the lateral discharge (Rq_0 decreases up to 4.5%); ii) towards the upstream wall, the
356 obstacle is usually located within the recirculation zone where it has no impact but as the width of this zone
357 reduces, the obstacle can block off part of the lateral discharge (Rq_0 decreases up to 3%). Such influence of
358 the location of the obstacles on the modifications of discharge distribution should be considered in flooded
359 urban areas for car park planning. Moreover, for a given obstacle, as the Froude number of the inflow
360 increases, the impact of the obstacle strongly increases. Oppositely, it appeared that the water depth in the
361 intersection has very limited influence on the impact of obstacles.

362 - For a given flow in which an obstacle is introduced, the impact on the discharge distribution is a
363 direct consequence of the modifications of the following flow structures: i) streamwise and centrifugal flow
364 acceleration, ii) width of the recirculation zone and iii) wake downstream the obstacle.

365 - Overall, the impact of the obstacles remains limited to about 10 to 15% of the inflow discharge even
366 for very high Froude number flows. However, considering a scale ratio of about 25 between the experimental
367 set-up and a real street (leading to a 7.5m wide street) and using a Froude similarity, the equivalent velocity
368 would reach 1 to 2 m/s and the Reynolds number 2×10^6 to 8×10^6 . Assuming a typical street roughness height
369 of 5 mm, the flow regime at the street scale will be hydraulically rough which may introduce some
370 discrepancies when transferring the present results to real urban flood cases. Moreover, this impact is
371 expected to increase with the size of obstacles, which is not covered in the present study. For flooding
372 consideration, 10% to 15% change can be substantial. It is recommended to include these singularities as
373 impervious areas within the topography of a city in 3D or 2D urban flood simulation or by a calibrated head
374 loss term in 1D network simulation.

375

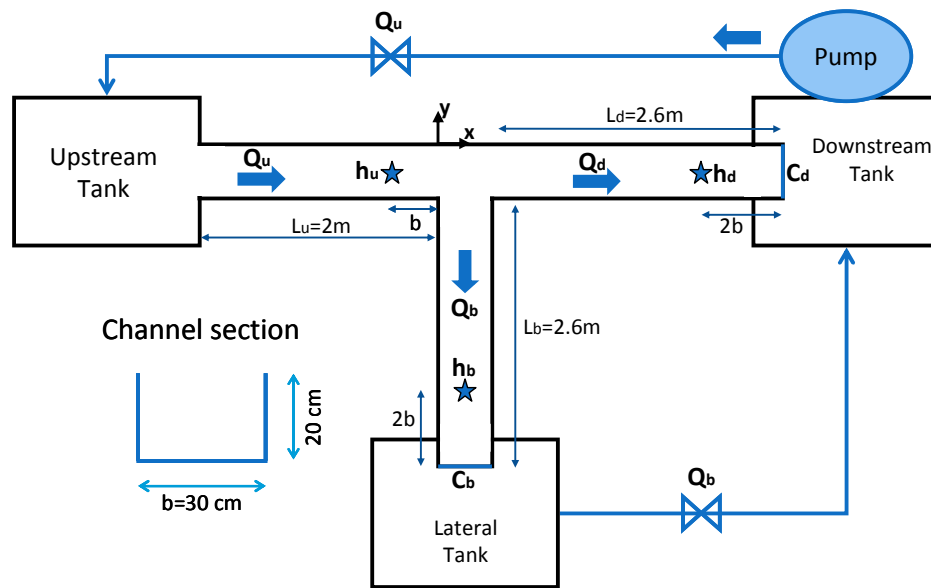
376 **5. Acknowledgements**

377 The work was supported by a grant from the PROCORE-France/Hong Kong Joint Research Scheme
378 sponsored by the Research Grants Council and the Consulate General of France in Hong Kong (2011, project
379 n°24664RB) and benefited from the support of the French CNRS, INSU, through grant EC2CO Cytrix 2011-
380 231.

381 **6. References**

382 Barkdoll, B.D., 1997. Sediment control at lateral diversions, PhD dissertation, Civil and Environmental
383 Engineering, University of Iowa, Iowa City, Iowa.
384 Bazin, P.H., Bessette, A., Mignot, E., Paquier, A., Riviere, N., 2012. Influence of detailed topography when
385 modeling flows in street junction during urban flooding. Journal of Disaster Research, 7 (5), 560-566.

- 386 Chen, D., Jirka, G.H., 1995. Experimental study of plane turbulent wakes in shallow water layer. Fluid
387 Dynamics Res. 16 (1), 11-41.
- 388 Li, C.W., Zeng, C., 2009. 3D Numerical modelling of flow divisions at open channel junctions with or
389 without vegetation, *Advances In Water Resources*, 32, 1, 49-60.
- 390 Li, C.W., Zeng, C., 2010. Flow division at a channel crossing with subcritical or supercritical flow. *Intern. J.*
391 *for Num. Methods in Fluids*. 62, 56-73.
- 392 Lin, P., Li, C.W., 2002. A sigma-coordinate three-dimensional numerical model for surface wave
393 propagation. *International Intern. J. for Num. Methods in Fluids*. 38, 1045-1068.
- 394 Mignot, E., Paquier, A., Ishigaki, T., 2006. Comparison of numerical and experimental simulations of a flood
395 in a dense urban area. *Water Science and Tech*. 54, 65–73.
- 396 Mignot, E., Riviere, N., Perkins, R.J., Paquier, A., 2008. Flow patterns in a four branches junction with
397 supercritical flow. *J. Hydr. Eng*. 134(6), 701–713.
- 398 Neary, V.S., Sotiropoulos, F., Odgaard, A.J., 1999. Three-dimensional numerical model of lateral-intake
399 inflows. *J. Hydr. Eng*. 125(2), 126–140.
- 400 Ramamurthy, A.S., Tran, D.M., Carballada, L.B., 1990. Dividing flow in open channels. *J. Hydr. Eng*.
401 116(3), 449–455.
- 402 Rivière, N., Perkins, R.J., Chocat, B., Lecus, A., 2006. Flooding flows in city crossroads: 1D modelling and
403 prediction. *Water Science and Techn*. 54(6-7), 75–82.
- 404 Riviere, N., Travin, G., Perkins, R.J., 2007. Transcritical flows in open channel in tersections. 32nd IAHR
405 Congress, 1-6 July 2007, Venice, Italy.
- 406 Riviere, N., Travin, G., Perkins, R.J., 2011. Subcritical open channel flows in four branch intersections.
407 *Water Resources. Res*. 47, W10517.
- 408

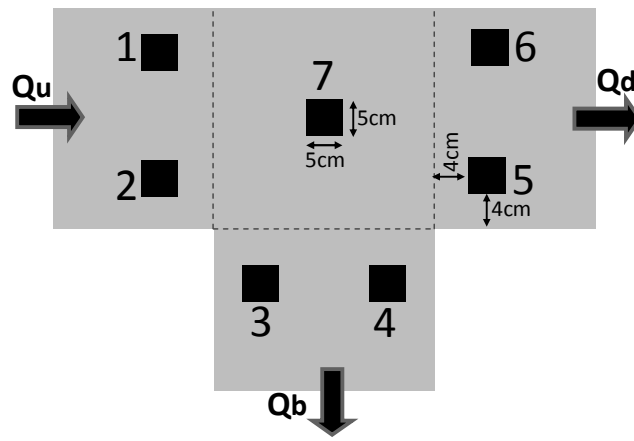


409

410

411

Figure 1: Scheme of the experimental set-up.



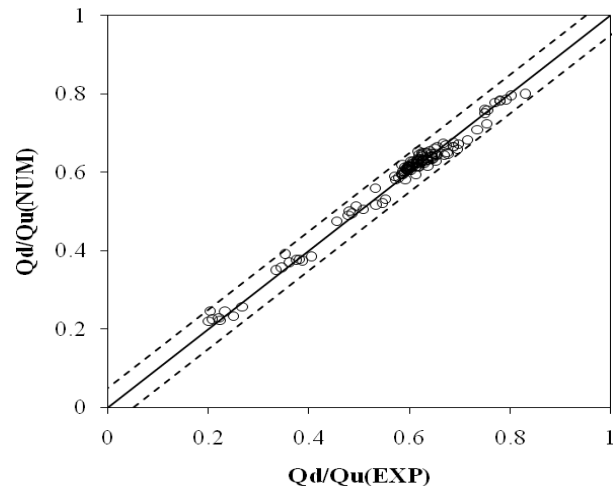
412

413

414

415

Figure 2: Location of the obstacles around the bifurcation.



416

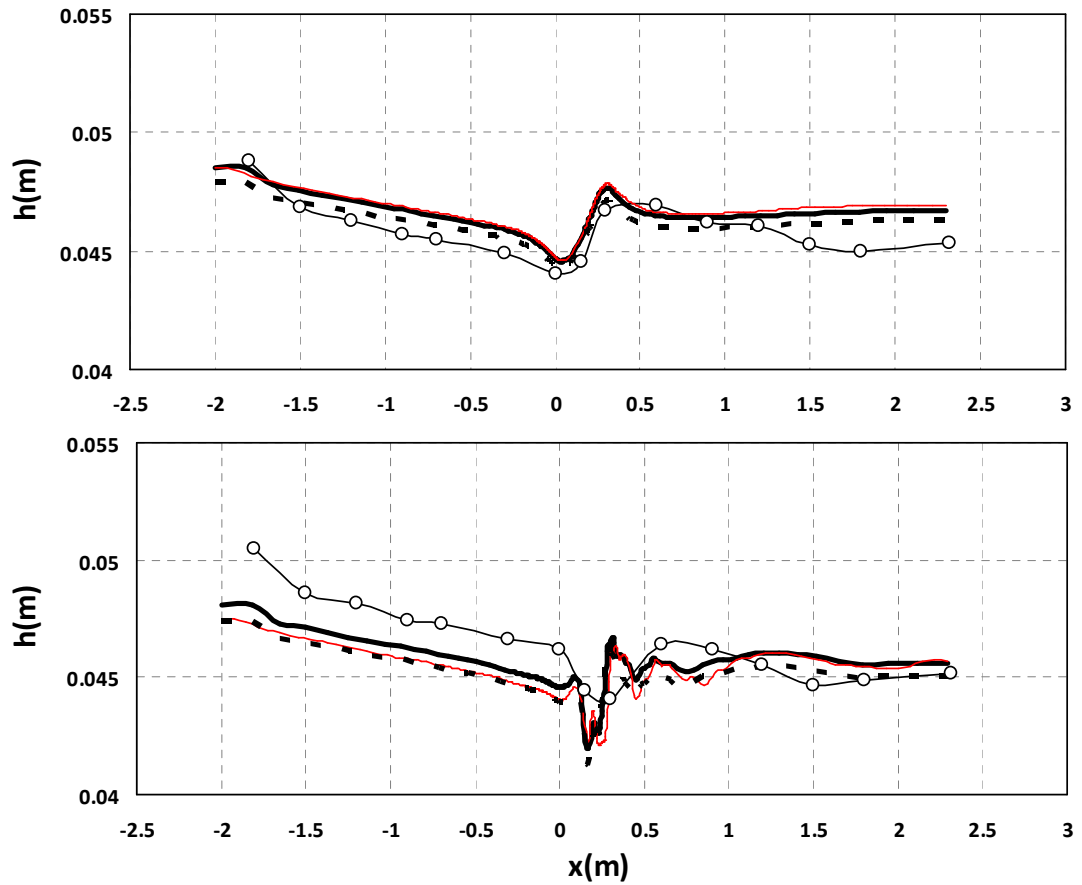
417

418

419

Figure 3: Comparison between measured (M) and computed (C) discharge ratios for the 14 flow x 10
obstacle configurations. Dotted lines refer to $\pm 5\%$ of Q_u

420



421

422

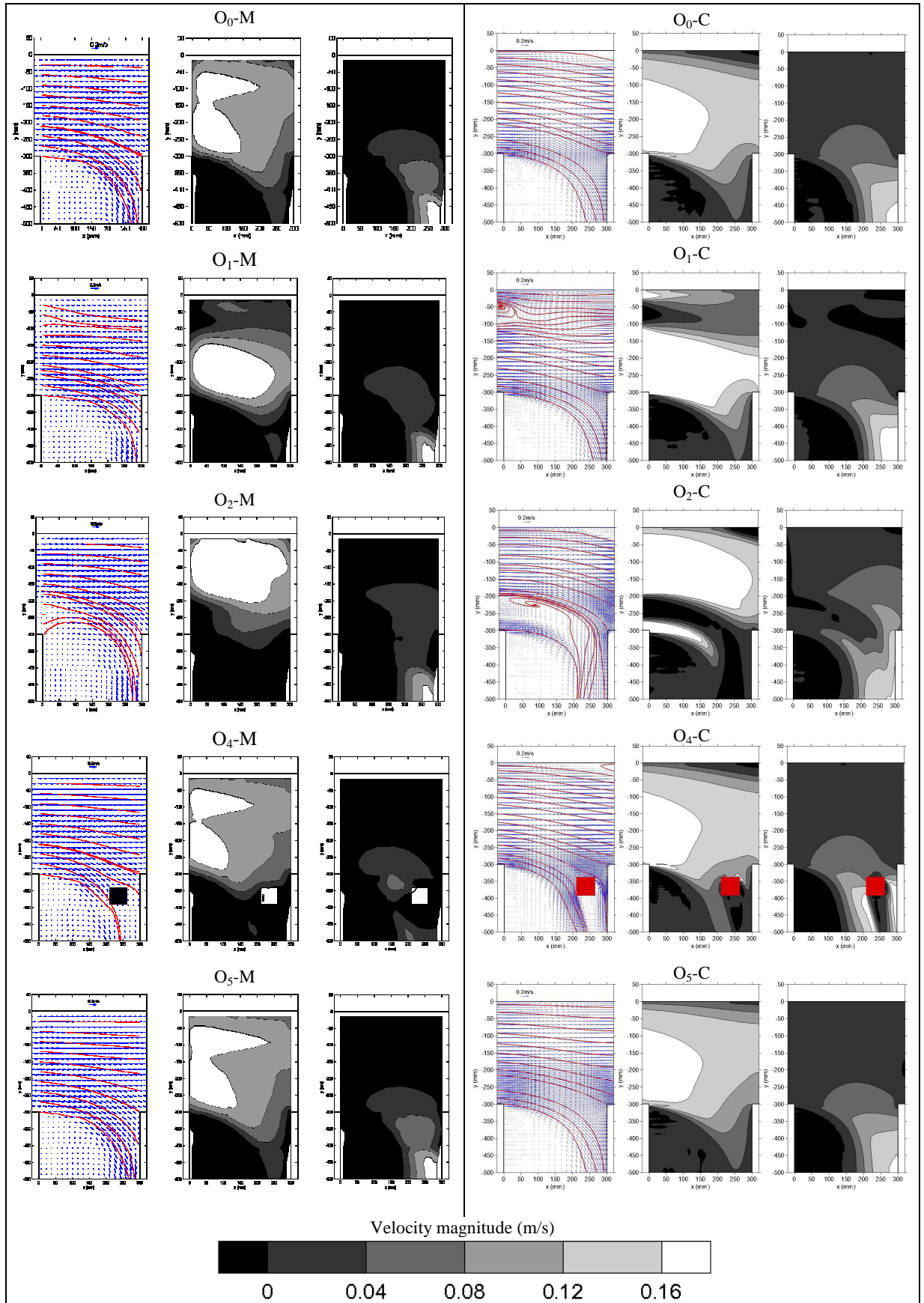
423

424

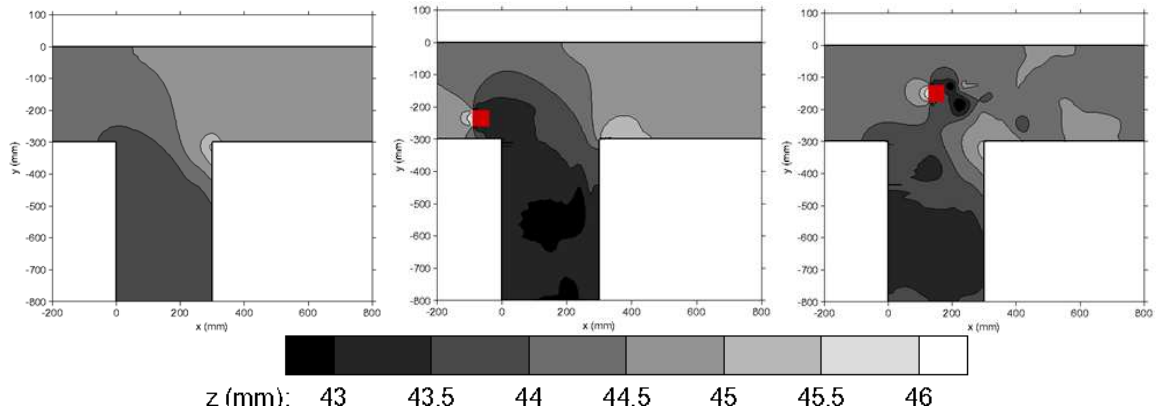
425

426

Figure 4: Measured (symbols) and computed backwater curves for the reference flow configuration (* in Table 1) along the main channel at $y=-0.22$ m without obstacle (O0, top) and with obstacle 7 (O7, bottom) using the reference numerical configuration (plain thick line), the refined mesh (red line) and the reference configuration with log profile at the inlet (dotted line).



430 Figure 5: Measured (M) and Computed (C) velocity fields at $z=3\text{cm}$ for bold flow in Table 1 without obstacle
431 (O_0) and with obstacle configurations 1, 2, 4, 5. For each flow: left graph = velocity field with streamlines;
432 center graph = u time-averaged velocity (along x axis); right graph = v time-averaged velocity (along y axis).
433



434

435

436

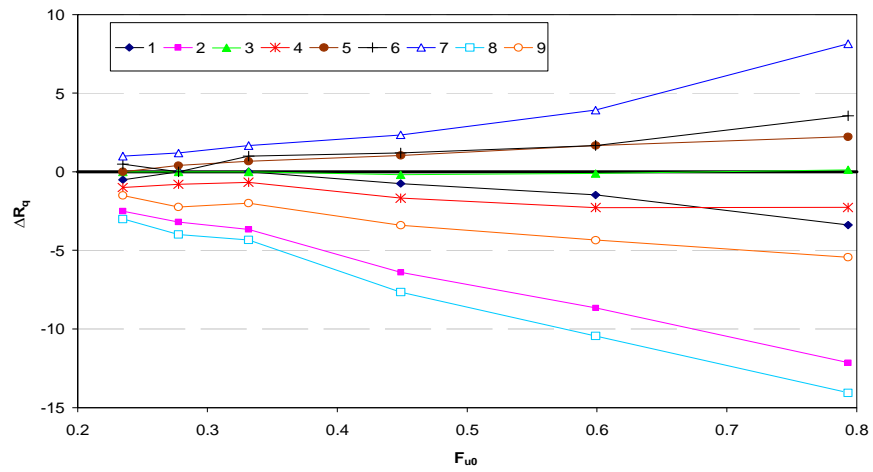
437

Figure 6: Computed free-surface elevation fields for bold flow in Table 1 without obstacle (O0) and with

438

obstacles O2 and O7.

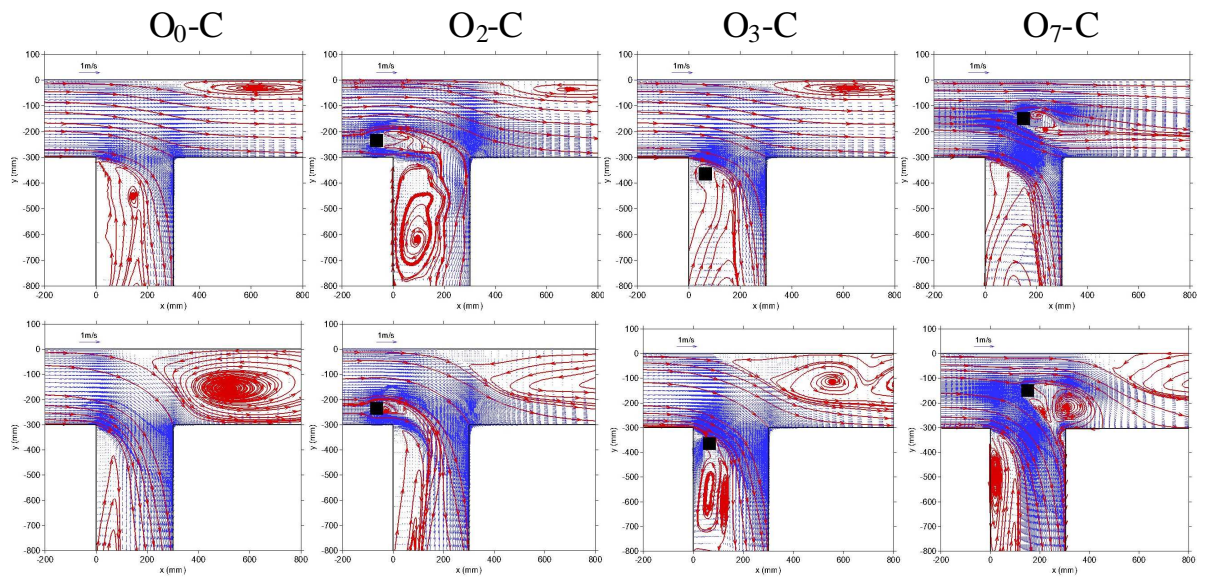
439



440

441 Figure 7: Measured impact of obstacles on the discharge distribution for flows in Serie 1 from Table 1 with
442 varying base upstream Froude numbers F_{u0} .

443



444

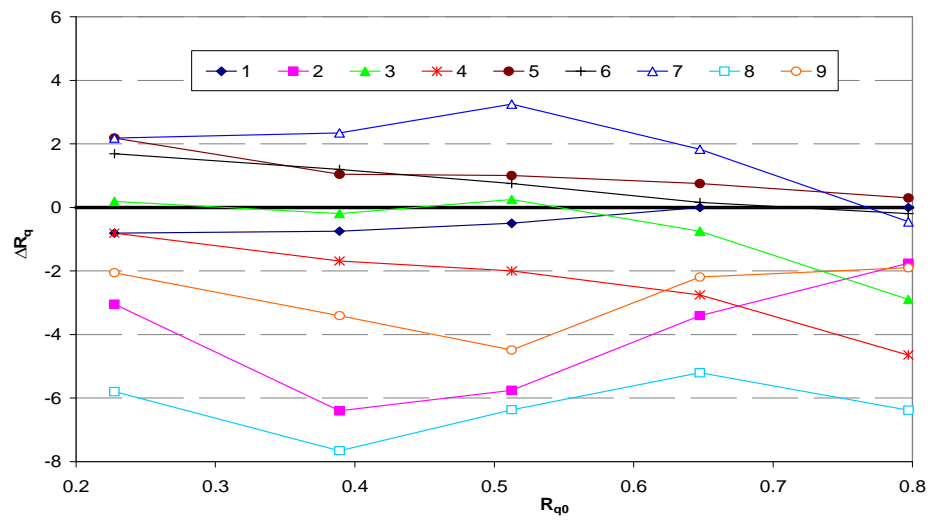
445 Figure 8: Computed velocity fields at $z=3\text{cm}$ with obstacle configurations 0, 2, 3 and 7 for $R_{q0}=0.39$ (top) and

446

$R_{q0}=0.8$ (bottom) in Serie 2 from Table 1.

447

448



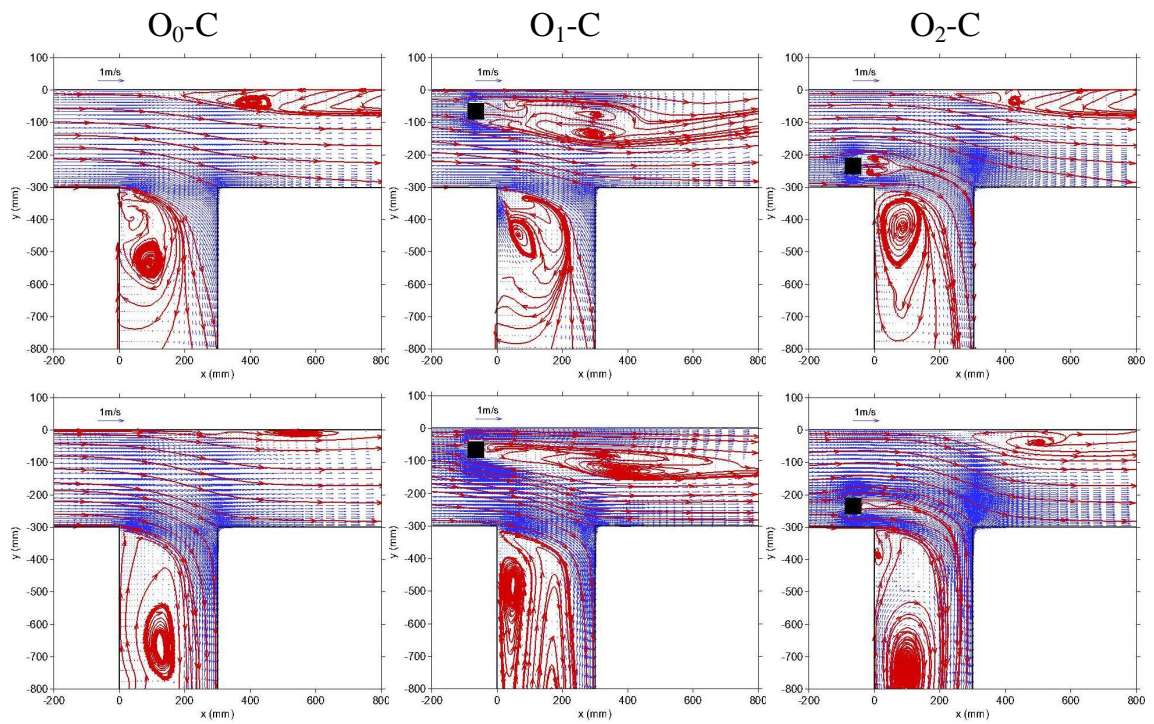
449

450

451

452

Figure 9: Measured impact of obstacles on the discharge distribution for flows in Serie 2 from Table 1 with varying base discharge distribution R_{q0}



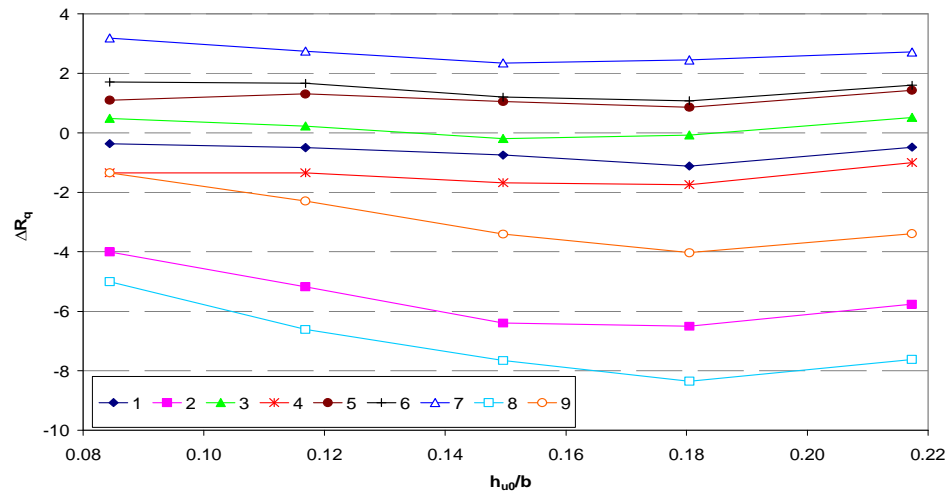
453

454 Figure 10: Computed velocity fields with obstacle configurations 0, 1 and 2 for $h_{u0}/b=0.08$ (top) and

455

$h_{u0}/b=0.22$ (bottom) in Serie 3 from Table 1.

456



457

458

Figure 11: Measured impact of obstacles on the discharge distribution for flows in Serie 3 from Table 1 with

459

varying base upstream water depths h_{u0}/b

460

461 Table 1: Non-dimensional parameters of the 14 flow configurations. The flow marked with an asterisk *
 462 (common to the three series) is referred to as the “reference configuration”. The first flow in bold, selected
 463 for velocity field measurement, is referred to as “PIV measured flow”.

Serie #	R_{u0}	F_{u0}	h_{u0}/b
	0.38	0.23	0.14
	0.40	0.28	0.15
S1	0.39	0.33	0.15
	0.39*	0.45*	0.15*
	0.39	0.60	0.14
	0.39	0.79	0.13
	0.23	0.44	0.15
S2	0.39*	0.45*	0.15*
	0.51	0.45	0.15
	0.65	0.44	0.15
	0.80	0.45	0.15
	0.40	0.44	0.08
S3	0.38	0.45	0.12
	0.39*	0.45*	0.15*
	0.39	0.45	0.18
	0.39	0.45	0.22

464

465

466 Table 2 Grid refinement study of discharge distribution for the reference flow configuration (* in Table 1).

No obstacle	Q_u (L/s)	R_q	h_u (mm)	h_d (mm)	h_b (mm)
Original	4	0.355	45.9	47.7	44.6
Fine grid	4.02	0.353	45.9	47.7	43.7

467

468

469 Table 3: Evolution of ΔR_q as R_{q0} increases (Serie S2)

Obstacle #	Low R_{q0} : sign of ΔR_q (Fig.8)	Evolution of ΔR_q as $R_{q0} \uparrow$ (Fig.10)
1	$< \mathbf{0}$	$\rightarrow \mathbf{0}$
2	$< \mathbf{0}$	$\rightarrow \mathbf{0}$
3	$\approx \mathbf{0}$	$\Delta R_{q3} < \mathbf{0}$
4	$< \mathbf{0}$	$\Delta R_{q4} \ll \mathbf{0}$
5-6	$> \mathbf{0}$	$\rightarrow \mathbf{0}$
7	$> \mathbf{0}$	$\rightarrow \mathbf{0}^*$
8	$< \mathbf{0}$	\approx
9	$< \mathbf{0}$	$\rightarrow \mathbf{0}$

470 * ΔR_{q7} becomes negative for $R_{q0} \geq 0.8$